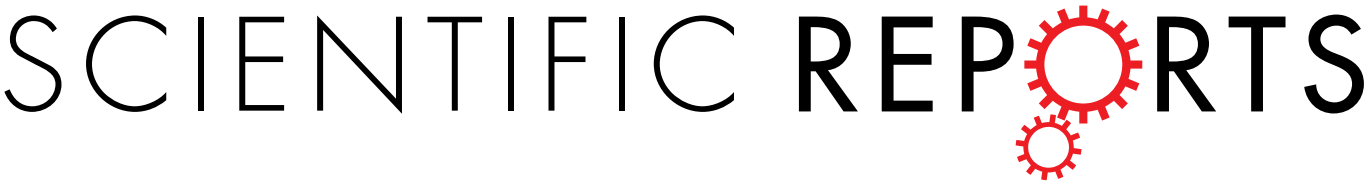

OPEN

Received: 24 September 2015
Accepted: 06 June 2016
Published: 29 June 2016

Propylene/propane permeation properties of ethyl cellulose (EC) mixed matrix membranes fabricated by incorporation of nanoporous graphene nanosheets

Bingbing Yuan[1,*], Haixiang Sun[1,2,*], Tao Wang[2], Yanyan Xu[2], Peng Li[1], Ying Kong[1] & Q. Jason Niu[1]

Nanopore containing graphene nanosheets were synthesized by graphene oxide and a reducing agent using a facile hydrothermal treatment in sodium hydroxide media. The as-prepared nanoporous graphene was incorporated into ethyl cellulose (EC) to prepare the mixed matrix membranes (MMMs) for C_3H_6/C_3H_8 separation. Transmission electron microscopy (TEM) photograph and X-ray photoelectron spectroscopy (XPS) analysis of nanoporous graphene nanosheets indicated that the structure of nanopore was irregular and the oxygen-containing groups in the surface were limited. More importantly, the as-prepared MMMs presented better separation performance than that of pristine EC membrane due to simultaneous enhancement of C_3H_6 permeability and ideal selectivity. The ideal selectivity of the MMMs with 1.125 wt‰ nanoporous graphene content for C_3H_6/C_3H_8 increased from 3.45 to 10.42 and the permeability of C_3H_6 increased from 57.9 Barrer to 89.95 Barrer as compared with the pristine membrane. The presumed facilitated mechanism was that the high specific surface area of nanoporous graphene in polymer matrix increased the length of the tortuous pathway formed by nanopores for the gas diffusion as compared with the pristine graphene nanosheets, and generated a rigidified interface between the EC chains and fillers, thus enhanced the diffusivity selectivity. Therefore, it is expected that nanoporous graphene would be effective material for the C_3H_6/C_3H_8 separation.

The separation of low-carbon olefin/paraffin mixtures is one of the most challenging tasks in the petrochemical industry due to their similar molecular sizes and physical properties. Currently, the separation is mainly achieved by fractional distillation at cryogenic temperature[1], and large capital investment and high energy consumption involved in this conventional technology stimulates the researchers to find a more cost-effective separation process[2]. As an alternatively energy-saving approach, membrane separation technology has a great potential in the petrochemical industry[3–5]. Mixed matrix membranes (MMMs) that are composed by blending inorganic particles into the polymer matrix are promising approaches; they combine the easy processing polymeric membranes with superior separation performance of inorganic nanoparticles[6]. These advantages also provide an opportunity to overcome the individual deficiencies of inorganic materials and polymers, offering attractive solutions for industrial applications. Correspondingly, there are several inorganic materials such as zeolites, carbon molecular sieves (CMS), carbon nanotubes (CNTs), C_{60}, metal-organic frameworks (MOFs), and covalent organic frameworks (COFs) that have been amalgamated into the polymer matrix to prepare the MMMs for gas separation, and subsequently achieved enhanced CO_2/CH_4, O_2/N_2, H_2/CO_2 and CO_2/N_2 selectivity[7–12].

In recent years, a few studies have been reported about employing mixed matrix platform to the C_3H_6/C_3H_8 system using nanofillers, and most nanofillers are spherical shape like silica materials and C_{60}, or square zeolitic like imidazolate framework ZIF-8 [13–15]. For example, Naghsh and Sadeghi[14] studied the separation of propylene/

[1]State Key Laboratory of Heavy Oil Processing, China University of Petroleum (East China), Qingdao 266580, P.R. China. [2]College of Science, China University of Petroleum (East China), Qingdao 266580, P.R. China. *These authors contributed equally to this work. Correspondence and requests for materials should be addressed to H.S. (email: sunhaixiang@upc.edu.cn) or Q.J.N. (email: qjniu@upc.edu.cn)

propane using cellulose acetate-silica nanocomposite membranes, and the selectivity for C_3H_6/C_3H_8 was 6.12 and the permeability of C_3H_6 was 0.098 Barrer with a nanocomposite membrane that contains 30 wt% silica particles under 2 bar feed absolute pressure and 35 °C temperature. Koros *et al.*[13] found that mixed matrix membranes, fabricated by 6FDA-DAM polyimide and ZIF-8, had an ideal selectivity of 31.0 for C_3H_6/C_3H_8, and a permeability of 56.2 Barrer for C_3H_6 with 48.0 wt% ZIF-8 loading, which were 150% and 258% higher than the pure 6FDA-DAM membrane respectively for selectivity and permeability.

As mentioned above, most available literatures focused on the spherical and square shape nanofillers to enhance the gas separation performance. It is inevitable to generate the 'sieve-in-a-cage morphology' between these nanofiller materials and polymer interface due to the low aspect ratio of the spherical and square shape nanofillers and the weak interfacial adhesion. Such voids decrease the selectivity of the MMMs, even the permeability is increased[7,16]. In contract, the graphene nanosheets are intrinsically more compatible with polymers as compared to other quadrate or sphere molecule sieves because of its high aspect ratio (>1000), easy surface functionalization, and high thermal and mechanical properties[17,18]. Moreover, the high specific surface area fillers in the polymer matrix increase the length of the tortuous pathway for gas diffusion and reduce the mobility of polymer chains. This advantage will restrict the diffusion of larger molecules, and favor the diffusion of small molecules with less resistance, thus improving gas diffusivity selectivity[19–24]. On the other hand, Checchetto *et al.*[25] studied the gas transport performance of nanocomposite membrane that was composed of polyethylene with dispersed graphite nanoplatelets (GNPS), and the results indicated that GNPS with nominal content of 5 wt% inclusions reduced the permeability by approximately a factor of two as compared with that of pure polymer membrane. This was due to the fact that the defect-free graphene and its derivatives like graphene oxide were theoretically gas impermeable, and such ultrathin two dimensional structure hindered gas diffusion, which was consistent with the theoretical compute studies that a perfect graphene was impermeable to gases even as small as He[26,27]. Therefore, it is useful to fabricate nanopores in the graphene nanosheets to further enhance the tortuous pathway of small gas molecule diffusion and hinder the big gas molecule diffusion in the polymer matrix.

For the reasons discussed above, ethyl cellulose (EC) is selected in this study as the polymer matrix based on its comparatively large free volume and relatively low glass transition temperatures, which might provide high gas permeability and a superb C_3H_6 diffusion coefficient. Furthermore, massive oxygen functional groups on the surface of graphene nanosheets generate better interfacial bonding strength with EC polymer[28–30]. To be specific, the nanoporous graphene was synthesized by sodium hydroxide using a facile hydrothermal treatment, and then the MMMs were fabricated with the addition of nanoporous graphene into EC polymer through solution blending method. In order to prove the nanopores in the surface of graphene nanosheets are beneficial for the enhancement of C_3H_6/C_3H_8 separation performance, light reduction graphene oxide (L-rGO) containing oxygen-containing groups such as carboxyl, hydroxyl group and reduction graphene oxide (rGO) were synthesized and incorporated into EC polymer to prepare MMMs for C_3H_6/C_3H_8 permeation. The morphology and microstructure of the as-prepared graphene material were confirmed, and the physical properties of MMMs in terms of microstructure, crystallization, tensile property and thermal stability (see Supplementary Information Table S1 and Fig. S3) were investigated as well. Moreover, for nanoporous graphene MMMs, the effects of feed pressure on the C_3H_6/C_3H_8 permeation performance were systematically examined and evaluated (see Supplementary Information Fig. S4 and Fig. S5).

Results and Discussion

Characterization of the L-rGO, rGO and nanoporous rGO nanosheets. Different methods of treatment on GO nanosheets may result various morphologies, and these changes can be directly observed through TEM characterization. Figure 1 shows the TEM images of L-rGO, rGO and nanoporous rGO nanosheets. As shown in Fig. 1(a), L-rGO presents relatively smooth nanosheets in comparison with rGO and nanoporous rGO nanosheets, since that trace amount of $NaBH_4$ is inadequate for the chemical reduction of the vast oxygen groups on the GO nanosheets. However, intensive deoxygenation processes can be completed with abundant $NaBH_4$ reduction and NaOH hydrothermal treatment, as shown in Fig. 1(b,c). The nanopores with irregular shapes are clearly distributed on the nanoporous rGO nanosheets, indicating that substantial decarbonisation and violent deoxygenation process had occurred during the hydrothermal treatment. In contrast, the rGO nanosheets practically exhibit no obvious nanopores and merely wrinkled texture, due to the deletion of oxygen groups[31]. The nanopores on the surface of rGO nanosheets may increase the specific surface area and the length of the tortuous pathway for the gas diffusion in the EC polymer matrix. In addition, the graphene nanosheets with high-aspect ratio may also contribute to the polymer and graphene nanosheets in the formation of MMMs with excellent permeability performance and mechanical properties.

Variation on the morphologies of graphene nanosheets can also be indirectly measured by the Raman spectra. As observed in Fig. 2, from L-rGO to rGO, and then nanoporous rGO nanosheets, it is clearly observed that the intensity of D band gradually increases as compared with G band, and the intensity of G band marginally decreases[32,33]. During the chemical reduction process, the average size of sp^2 regions in the graphene were gradually weakened and resulted in a defected surface. After that, these defected sites increasingly expanded and finally generated nanopores in the intensive hydrothermal treatment process. Therefore, an increased I_D/I_G intensity ratio gradually emerges from light chemical reduction (L-rGO) to chemical reduction (rGO), and then hydrothermal treatment (nanoporous rGO). Combined with the results of TEM images, it can be concluded that nanoporous rGO nanosheets would contain large amount of nanopores as compared with L-rGO and rGO nanosheets.

The micro-structure of graphene nanosheets were also characterized by FTIR spectroscopy. As shown in Fig. 3(a), the peaks at around 1072, 1552, and 3401 cm^{-1} wavenumber are ascribed to the C–O, C=C and O–H groups in the L-rGO with a relative higher intensity in comparison with the rGO and nanoporous rGO nanosheets[34,35]. On the other hand, the appearance of asymmetric bands for the alkyl groups at 2917 and 2837 cm^{-1}

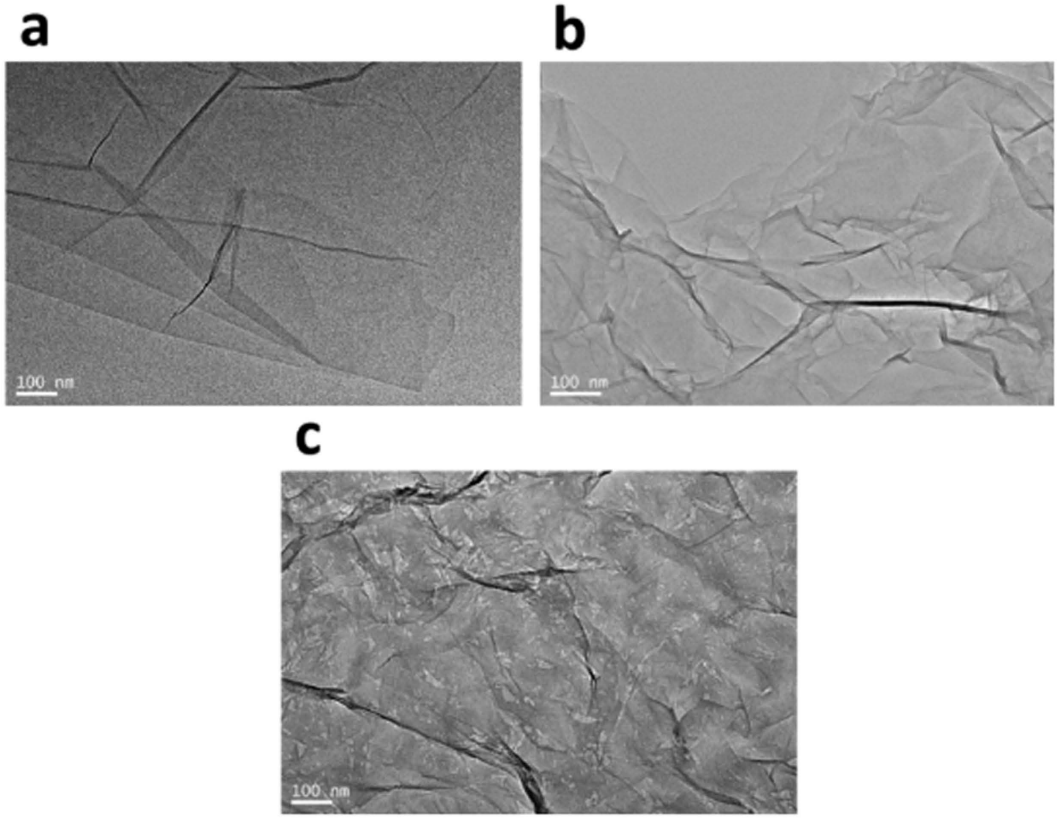

Figure 1. TEM images of the L-rGO nanosheets prepared under GO and $NaBH_4$ mass ratio 1:2 at 80 °C for 0.5 h (**a**); the rGO nanosheets prepared under GO and $NaBH_4$ mass ratio 1:25 at 80 °C for 2 h (**b**) and the nanoporous rGO nanosheets prepared using hydrothermal treatment (**c**).

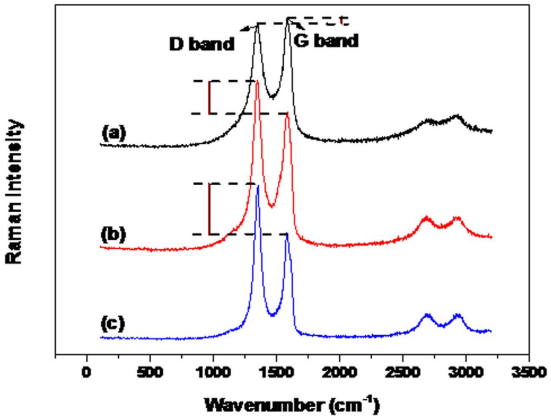

Figure 2. The Raman images of L-rGO nanosheets (**a**); rGO nanosheets (**b**) and nanoporous rGO nanosheets (**c**).

in rGO and nanoporous rGO results from the greatly decrease of the oxygen functional groups, indicating the completion of chemical reduction process.

In order to further confirm the difference of micro-structure of L-rGO, rGO and nanoporous rGO nanosheets, XPS measurement was conducted (Fig. 4). As shown in Fig. 4a, the C1s XPS spectrum of L-rGO clearly indicates a considerable degree of oxidation with four components which correspond to carbon atoms in different oxygen functional groups: the non-oxygenated ring C, the C in C–O bonds, the carbonyl C, and the carboxylate carbon (O–C=O)[36]. Moreover, L-rGO has a much lower peak intensity as compared with the C1s spectrum of rGO (Fig. 4b) and nanoporous rGO (Fig. 4c), despite possess the same oxygen functionalities. Figure 4d shows the direct atomic ratios (C1s/O1s) of L-rGO, rGO and nanoporous rGO, which also demonstrates the decrease of oxygen functionalities intensities. In addition, it is observed that rGO nanosheets exhibit lower oxygen functional intensity than that of nanoporous rGO, which are consistent with the results of FTIR.

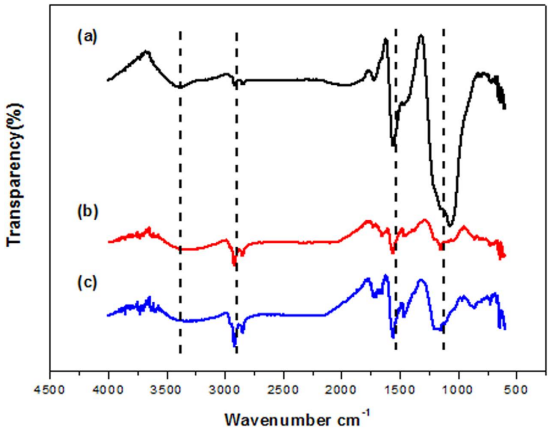

Figure 3. FTIR spectra of L-rGO nanosheets (**a**); rGO nanosheets (**b**) and nanoporous rGO nanosheets (**c**).

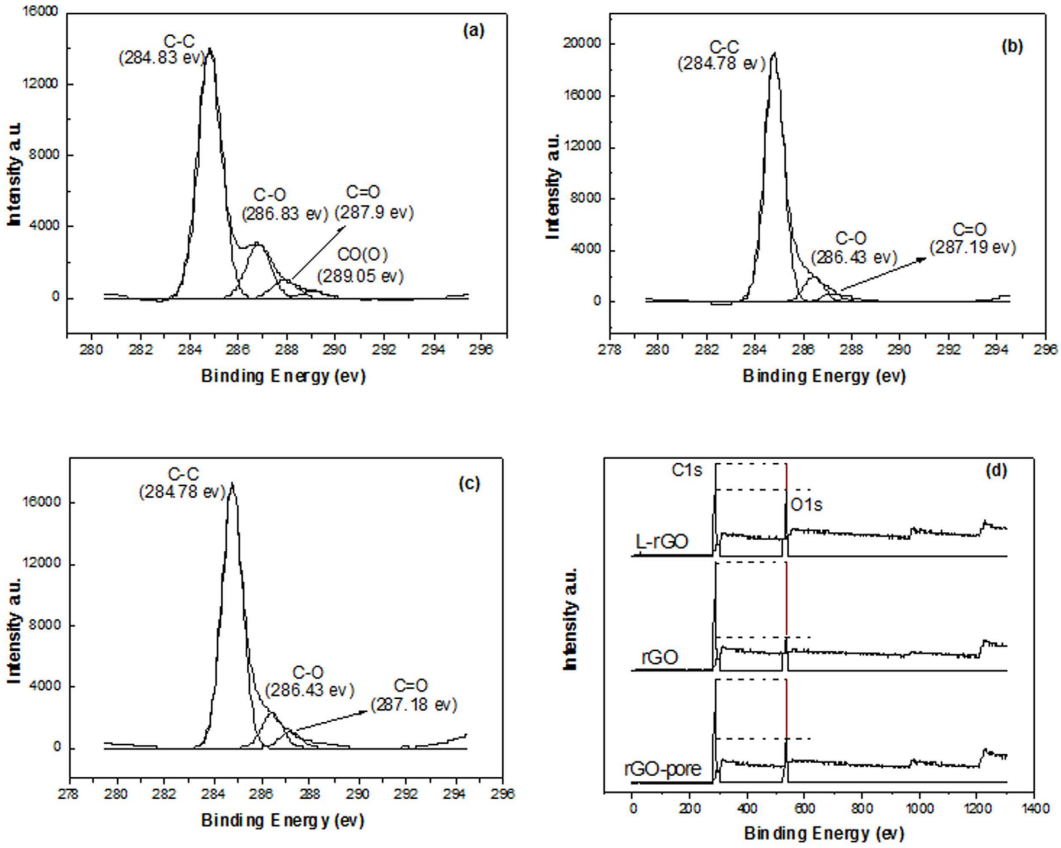

Figure 4. XPS spectra of L-rGO nanosheets (**a**), rGO nanosheets (**b**), nanoporous rGO nanosheets (**c**) and their XPS scan spectra (**d**).

Figure 5 shows the XRD patterns of L-rGO, rGO and nanoporous rGO nanosheets. The typical peak at $2\theta = 11.6°$ is attributed to the (002) plane of GO and $2\theta = 23.2°$, and is the characteristic of the parallel graphene layers, indicating that L-rGO, rGO and nanoporous rGO sheets are present both the consistent layers and the size of crystallite[37]. Furthermore, morphology and micro-structure confirm that three graphene nanosheets exhibit different oxygen-containing functional groups and nanopores, that is, L-rGO nanosheets with large amounts of oxygen functional groups in the surface, rGO nanosheets with predominant aromatic rings structure in the surface, and nanoporous rGO nanosheets with aromatic rings structure and nanopores in the surface. Meanwhile, the consistent layers and the size of crystallite also show that three graphene nanosheets are no difference except oxygen functional groups and nanopores.

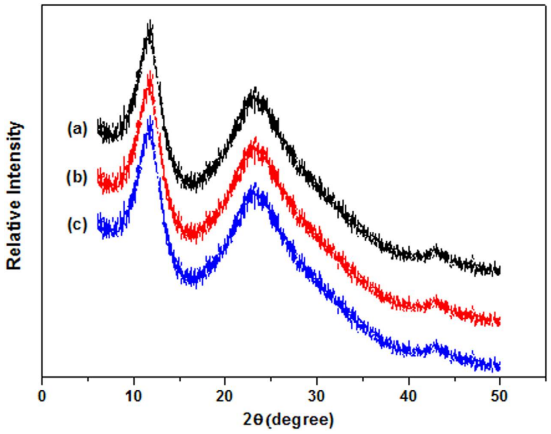

Figure 5. XRD patterns of L-rGO nanosheets (**a**); rGO nanosheets (**b**) and nanoporous rGO nanosheets (**c**).

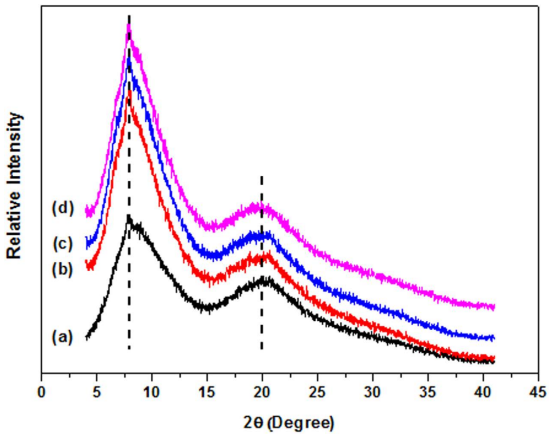

Figure 6. XRD patterns of pure EC membrane (**a**); L-rGO MMMs (**b**); rGO MMMs (**c**) and nanoporous rGO MMMs (**d**).

Membrane Characterization. XRD is performed to investigate the effects of graphene nanosheets on the EC polymer chains. As shown in Fig. 6, the representative diffraction peaks of L-rGO, rGO and nanoporous rGO nanosheets were disappeared. Moreover, Fig. 6 also provides that the graphene nanosheets have a slight impact on the diffraction patterns of the EC polymer, especially on the variation of interlayer distance. Diffraction peaks at 2θ (°) of 7.93 and 20.56 are the characteristic of cholesteric liquid crystallinity. The small angle peak at 2θ (°) of 20.56 attributes to the interlayer distance of the ordered chains of the EC polymer, with the second peak reflecting the interchain distance[38,39], therefore, graphene nanosheets have no influence on the interlayer and interchain distance of EC polymer matrix. On the other hand, the diffraction peak at 2θ (°) of 7.93 in L-rGO, rGO and nanoporous rGO nanosheets has an increased intensity as compared with that of pure EC, indicating an enhanced crystalline arrangement of EC chains. In this case, the incorporation of nanofillers into the EC polymer matrix generates a rigid interface between EC chains and graphene nanosheets, which hinders the mobility of macromolecular segments resulted from an increased chains crystallinity[40,41], and eventually decreases the free volumes among polymer chains.

The cross-section morphologies of three MMMs are presented in Fig. 7. It can be observed that the PI ultrafiltration membrane presents a larger finger-like pore structure, which is unfavorable for the permeation of gas. Furthermore, the morphology of membrane has no significant change among EC membrane and MMMs, indicating a superb compatibility between graphene nanosheets and EC polymer[42,43]. Magnified images of cross-section morphologies are shown in Fig. 7(b,d,f,h). It is evident that no nanofillers are distinguished and MMMs are relatively flatter than that of EC, which indicates that graphene nanosheets are well dispersed in EC polymer matrix. According to Fig. 6, incorporation of nanofillers into the EC polymer matrix hinders the mobility of macromolecular segments and increases its chains crystallinity, thus graphene nanosheets can act as a nucleating agent in the polymer membranes[44–46]. The excellent dispersion and compatibility was observed, since graphene nanosheets with high aspect ratio can increase the interfacial area between EC polymer chains and nanosheets, resulting in a better compatibility and dispersion in polymer matrix.

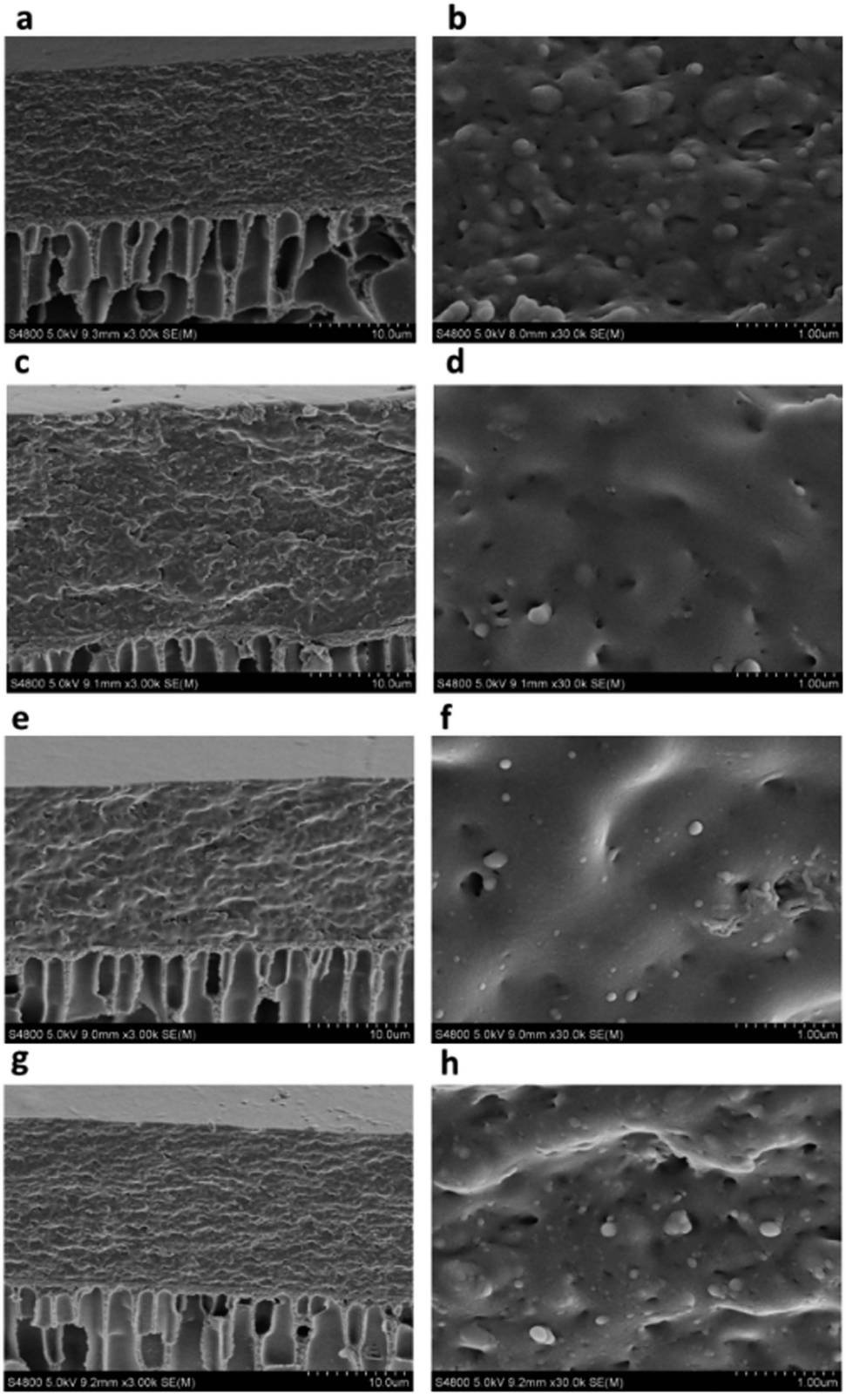

Figure 7. SEM images of cross-section of pure EC membrane (**a,b**), L-rGO MMMs (**c,d**), rGO MMMs (**e,f**) and nanoporous rGO MMMs (**g,h**).

The TEM image of nanoporous rGO MMMs solution further verifies the nanoscale morphology of nanoporous rGO nanosheets. As observed in Fig. 8, a relatively ambiguous morphology of nanoporous graphene nanosheets was observed in nanoporous rGO in MMMs, probably due to the existence of EC chains. Moreover,

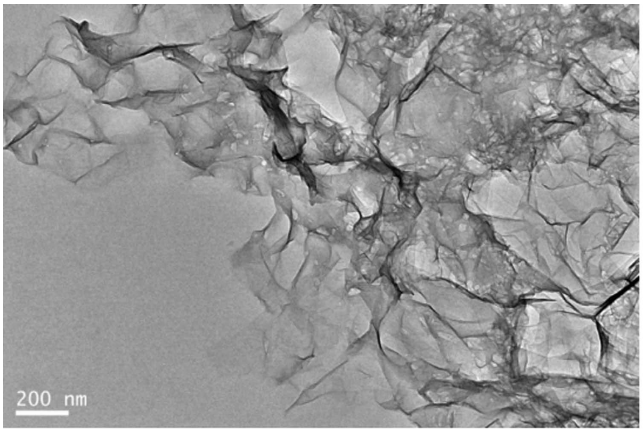

Figure 8. TEM image of nanoporous rGO nanosheets in the MMMs solution.

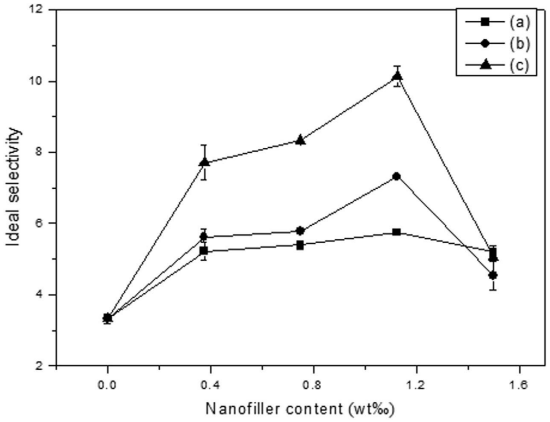

Figure 9. Effect of graphene nanosheets content in the EC polymer matrix on the C_3H_6/C_3H_8 ideal selectivity: (**a**) L-rGO MMMs; (**b**) rGO MMMs; (**c**) nanoporous rGO MMMs. (Feed pressure at 0.1 MPa, temperature at 298 K).

it can be clearly seen that there are plenty of nanopores in the nanoporous rGO nanosheets, and these nanopores are facile channels for the small gas molecules to permeate. These phenomena are complementary with the TEM images of nanoporous rGO nanosheets described in the earlier section.

Membrane permeation performance. In order to investigate the structure of graphene nanosheets and their loading content on the membrane permeation performances, three kinds of MMMs are fabricated with different nanofiller loading. Figures 9 and 10 present the correlation between the ideal selectivity and permeability with different loading of graphene nanosheets in the EC polymer matrix. As shown in Figs 9 and 10, C_3H_6 permeability, C_3H_6/C_3H_8 ideal selectivity gradually increase with the increase of graphene nanosheets content from 0 to 1.125 wt‰, while C_3H_8 permeability decreases with the content of graphene nanosheets increase from 0 to 0.375 wt‰ and then remain unchanged after 0.0375 wt‰ of graphene nanosheets loading. However, when the loading of the graphene nanosheets in the EC polymer matrix increases to 1.5 wt‰, both C_3H_6 permeability and C_3H_6/C_3H_8 ideal selectivity decrease, indicating that the graphene nanosheets are theoretically impermeable to all atoms and molecules, and greater loading in the MMMs could cause the agglomeration of the graphene nanosheets, resulting in the decrease of the effective surface area[47–50]. With 1.125 wt‰ of L-rGO, rGO and nanoporous rGO nanosheets loading in the EC polymer matrix, the ideal selectivity of the MMMs could reach as high as 5.74, 7.29 and 10.42 with C_3H_6 permeability of 66.05, 76.34 and 89.95 Barrer, respectively. Meanwhile, it is clearly showed that the ideal selectivity of pure EC polymer membrane is 3.45 and the permeability of C_3H_6 and C_3H_8 is 57.9 and 16.78 Barrer, which is consistence with the related literature[51]. The notable increment involved in both C_3H_6 permeability of 1.55-fold and C_3H_6/C_3H_8 ideal selectivity of 3.02-fold confirm the fact that the nanopores blended into the MMMs enhance the C_3H_6 permeability as compared with the pure EC membrane gas permeation performance. However, the blending of graphene nanosheets into the EC polymer matrix hinders the C_3H_8 permeability. Among three kinds of MMMs, nanoporous graphene MMMs have C_3H_6/C_3H_8 ideal selectivity and C_3H_6 permeability advantages over that of L-rGO and rGO MMMs, which indicates that oxygen-containing functional groups decrease the C_3H_6 permeability. A reasonable explanation of the gas separation mechanism is

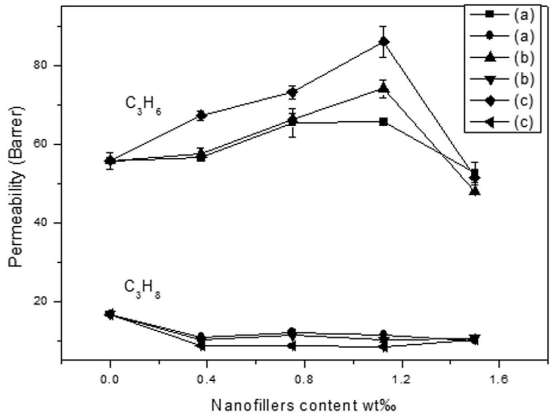

Figure 10. Effect of three graphene nanosheets content in EC polymer matrix on the permeability of C_3H_6 and C_3H_8: (**a**) L-rGO MMMs; (**b**) rGO MMMs; (**c**) nanoporous rGO MMMs. (Feed pressure at 0.1 MPa, temperature at 298 K).

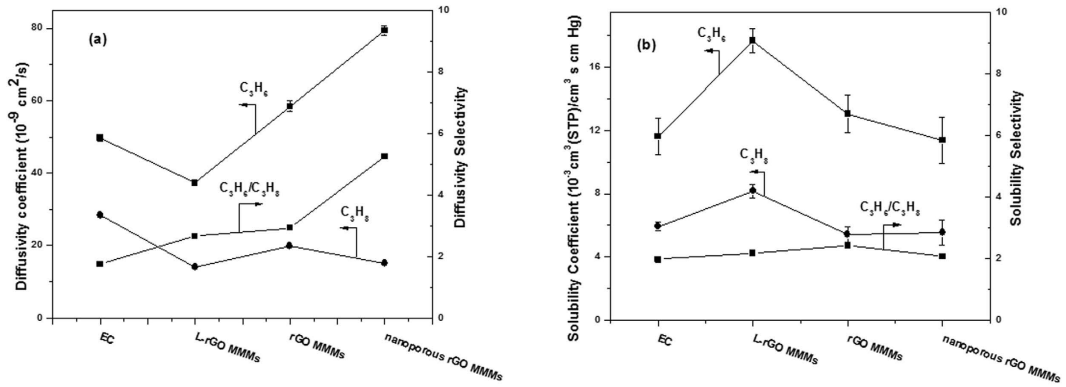

Figure 11. Diffusion coefficient (**a**) and solubility coefficient (**b**) of C_3H_6 and C_3H_8 in the membranes. (Feed pressure at 0.1 MPa, temperature at 298 K).

proposed as shown in Fig. S6, and 1.125 wt‰ of nanofiller loading is chosen as the optimal loading in MMMs for the further discussion of gas permeation properties.

To further explore the effect of nanopore in the graphene nanosheets on the gas permeation performance, the diffusivity coefficient (D) and solubility coefficient (S) of the membranes with the optimal 1.125 wt‰ of nanofiller loading are compared in Fig. 11. As shown in Fig. 11(a), it is found that C_3H_6/C_3H_8 diffusivity selectivity of L-rGO MMMs, rGO MMMs and nanoporous rGO MMMs are higher than that of pure EC membrane. It is notable that the nanoporous rGO MMMs has the highest C_3H_6/C_3H_8 diffusivity selectivity among L-rGO MMMs and rGO MMMs. The lack of nanopores in the nanosheets hinders the further enhancement of C_3H_6 diffusivity coefficient, even L-rGO nanosheets and rGO nanosheets generate a rigid interface with EC polymer chains and increase the tortuous pathway of the gas diffusion to enhance the diffusivity selectivity. We can conclude that the nanopores in the nanosheets further increase the tortuous pathway of the C_3H_6 diffusion with less resistance but restrain the diffusion of C_3H_8 molecules.

Figure 11(b) shows the gas solubility coefficients and C_3H_6/C_3H_8 solubility selectivity of L-rGO MMMs, rGO MMMs and nanoporous rGO MMMs with the optimal 1.125 wt‰ of nanofiller loading. The solubility of C_3H_6 and C_3H_8 in the polymer membranes depends on their relative condensability, characterized by critical temperature, the interaction between polymer and gases, the fraction and amount of free volumes in glassy polymers. The critical temperatures of C_3H_6 and C_3H_8 are in the following order: C_3H_6(364.76 K) < C_3H_8(369.8 K). It is believed that higher condensability has the higher solubility of gas in the polymer matrix[52–55], however, C_3H_6 exhibits greater solubility than C_3H_8. This is thanks to the high electron cloud on the double bond with high polarity and flat structure, resulting in more affinity of C_3H_6 to generate interaction with polymer, and thus enhancing the C_3H_6 solubility. Moreover, the incorporation of graphene nanosheets increases the density of polar groups such as -COOH and -OH in the MMMs. As a result, it creates polar spaces between the interface of nanofillers and polymer. This formation of polar spaces would result in the enhancement in the solubility coefficient of condensable gases[56].

The diffusivity selectivity increases by 5.24-fold in comparison with 2.66-fold for L-rGO MMMs and 2.93-fold for rGO MMMs, although the loading of nanoporous graphene nanosheets in the polymer matrix cannot efficiently increase the solubility selectivity of the gases due to the decrease of the free volume of the glassy polymer.

The incorporation of nanoporous graphene nanosheets into the EC polymer matrix mainly affects the diffusivity selectivity of C_3H_6/C_3H_8 molecule to enhance the ideal selectivity of MMMs, due to the existence of nanopores and the formation of rigid interface.

In summary, nanoporous rGO nanosheets were successfully fabricated by sodium hydroxide using a facile hydrothermal treatment. The morphology and micro-structure of the nanoporous rGO material were confirmed by TEM and XPS measurement. Nanoporous rGO nanosheets were incorporated into the EC polymer matrix to prepare the MMMs for the C_3H_6/C_3H_8 permeation. The permselectivity of nanoporous rGO MMMs exhibits a significant increase with the simultaneous enhancement of diffusivity selectivity and solubility selectivity, especially the 5.24-fold increase of the diffusivity selectivity. This result indicates that nanoporous rGO nanosheets are superior in terms of enhancing the diffusivity selectivity of C_3H_6 gas molecule. The ideal selectivity for C_3H_6/C_3H_8 and the permeability coefficient for C_3H_6 exhibit a significant increase of 3.02-fold and 1.55-fold in comparison with the pristine EC membrane, respectively. This study shows that nanoporous rGO nanosheets can be effective nanofiller in the polymer matrix to enhance the C_3H_6/C_3H_8 permeability.

Methods

Materials. EC (Mw = 200,000) was purchased from Shanghai Reagent Corporation (China). Graphite oxide was obtained from Nanjing XFNANO Materials Tech Co. Ltd. (China). Sodium borohydride ($NaBH_4$), sodium hydroxide (NaOH), sodium dodecylbenzene sulfonates (SDBS), hydrochloric acid (HCl 36~38%), acetone and all other types of reactants were bought from Shanghai Chemical Co., Ltd. (China). The propylene (purity > 99.5%) and propane (purity > 99.9%) were purchased from KODI Gas Chemical Industry Co. Ltd. (Foshan, China).

Fabrication of LGO, rGO and nanoporous rGO nanosheets. In this case, GO colloidal solution (0.1 g in 150 mL deionized water) was obtained using a mild ultrasonic exfoliation method for 2 h. The above colloidal solution was centrifuged to remove the impurities under 8000 r min^{-1} for 10 min. The rGO and L-rGO nanosheets were obtained through chemical reduction with the mass ratio of GO and $NaBH_4$ 1:25 at 80 °C for 2 h and 1:2 at 80 °C for 0.5 h respectively. The reduction solutions were subsequently collected based on filtration, flushing with deionized water and ethanol, and then the resulting products were stored in ethanol at a given concentration (0.012 g in 15 mL ethanol).

The nanoporous rGO nanosheets were synthesized with the treatment of sodium hydroxide under hydrothermal condition. Firstly, GO colloidal solution (0.1 g in 150 mL deionized water) obtained from an mild ultrasonic exfoliation method for 2 h was chemically reduced to L-rGO using the GO to $NaBH_4$ mass ratio of 1:2 at 80 °C for 0.5 h, and then the above L-rGO was collected by filtration. Subsequently, 10 mL SDBS (0.086 mol L^{-1}) and 20 mL NaOH (12.5 mol L^{-1}) were successively added dropwise to form a 60 mL solution. After stirred for 0.5 h, the reaction solution was decanted into a 100 mL Teflon-lined stainless steel autoclave and conducted the hydrothermal treatment at 180 °C for 3 h. Eventually, the reaction solution was cooled to ambient temperature, and the resulting solution was consecutively filtered and washed with sufficient deionized water (five times) and ethanol, and the nanoporous rGO nanosheets were placed in ethanol at a given concentration (0.012 g in 15 mL ethanol).

Fabrication of MMMs. A series of different concentration of L-rGO, rGO and nanoporous rGO ethanol solutions were prepared via sonication for 1 h. Dried EC (in a vacuum situation at 40 °C for 24 h) was dissolved in methylbenzene to form a solution with the concentration of 19.7 wt%. Under a nitrogen atmosphere and at ambient temperature, the above dispensed graphene ethanol solutions were then added dropwise to the EC solutions with stirring, The resulting casting solution had a mass ratio of graphene to EC of 0.375, 0.75, 1.125 and 1.5 wt‰ respectively. After 24 h dissolution, the casting solutions were filtered with stainless steel filter, and still degassing for 24 h. The above casting solution was then cast onto the polyimide (PI) ultrafiltration supported membrane using a micrometer film applicator under RH 40% at 298 K. The final membranes were subsequently preserved for gas separation tests. All membrane thicknesses were approximately 15–20 μm.

References

1. Baker, R. W. Future directions of membrane gas separation technology. *Ind. Eng. Chem. Res.* **41,** 1393–1411 (2002).
2. Eldridge, R. B. Olefin/paraffin separation technology: a review. *Ind. Eng. Chem. Res.* **32,** 2208–2212 (1993).
3. Stern, S. A. Polymers for gas separation: the next decade. *J. Membr. Sci.* **94,** 1–65 (1994).
4. Burns, R. L. & Koros, W. J. Defining the challenges for C_3H_6/C_3H_8 separation using polymeric membranes. *J. Membr. Sci.* **211,** 299–309 (2003).
5. Ravanchi, M. T., Kaghazchi, T. & Kargari, A. Application of membrane separation processes in petrochemical industry: a review. *Desalination* **235,** 199–244 (2009).
6. Moore, T. T., Mahajan, R., Vu, D. Q. & Koros, W. J. Hybrid membrane materials comprising organic polymers with rigid dispersed phases. *AIChE J.* **50,** 311–321 (2004).
7. Mahajan, R., Burns, R., Schaeffer, M. & Koros, W. J. Challenges in forming successful mixed matrix membranes with rigid polymeric materials. *J. Appl. Polym. Sci.* **86,** 881–890 (2002).
8. Tin, P. S., Chung, T. S., Jiang, L. & Kulprathipanja, S. Carbon–zeolite composite membranes for gas separation. *Carbon* **43,** 2025–2027 (2005).
9. Clarizia, G., Algieri, C. & Driolia, E. Filler-polymer combination: a route to modify gas transport properties of a polymeric membrane. *Polymer* **45,** 5671–5681 (2004).
10. Ismail, A. F., Kusworo, T. D. & Mustafa, A. Enhanced gas permeation performance of polyethersulfone mixed matrix hollow fiber membranes using novel Dynasylan Ameo silane agent. *J. Membr. Sci.* **319,** 306–312 (2008).
11. Zhang, Y., Musselman, I. H., Ferraris, J. P. & Balkus, Jr. K. J. Gas permeability properties of mixed-matrix Matrimid membranes containing a carbon aerogel: A material with both micropores and mesopores. *Ind. Eng. Chem. Res.* **47,** 2794–2802 (2008).
12. Perez, E. V., Balkus, Jr. K. J., Ferraris, J. P. & Musselman, I. H. Mixed-matrix membranes containing MOF-5 for gas separations. *J. Membr. Sci.* **328,** 165–173 (2009).
13. Zhang, C., Dai, Y., Johnson, J. R., Karvan, O. & Koros, W. J. High performance ZIF-8/6FDA-DAM mixed matrix membrane for propylene/propane separation. *J. Membr. Sci.* **389,** 34–42 (2012).

14. Naghsh, M., Sadeghi, M., Moheb, A., Chenar, M. P. & Mohagheghian, M. Separation of ethylene/ethane and propylene/propane by cellulose acetate-silica nanocomposite membranes. *J. Membr. Sci.* **423–424,** 97–106 (2012).
15. Sun, H. *et al.* Preparation and characterization of C_{60}-filled ethyl cellulose mixed-matrix membranes for gas separation of propylene/propane. *Chem. Eng. Technol.* **37,** 611–619 (2014).
16. Chung, T.-S., Jiang, L. Y., Li, Y. & Kulprathipanja, S. Mixed matrix membranes (MMMs) comprising organic polymers with dispersed inorganic fillers for gas separation. *Prog. Polym. Sci.* **32,** 483–507 (2007).
17. Bai, H., Li, C., Wang, X. & Shi, G. A pH-sensitive graphene oxide composite hydrogel. *Chem. Commun.* **46,** 2376–2378 (2010).
18. Li, H. *et al.* Ultrathin, molecular-sieving graphene oxide membranes for selective hydrogen separation. *Science* **342,** 95–98 (2013).
19. Zulhairun, A. K. & Ismail, A. F. The role of layered silicate loadings and their dispersion states on the gas separation performance of mixed matrix membrane. *J. Membr. Sci.* **468,** 20–30 (2014).
20. Du, N. *et al.* Polymer nanosieve membranes for CO_2-capture applications. *Nat. Mater.* **10,** 372–375 (2011).
21. Galve, A. *et al.* Combination of ordered mesoporous silica MCM-41 and layered titanosilicate JDF-L1 fillers for 6FDA-based copolyimide mixed matrix membranes. *J. Membr. Sci.* **431,** 163–170 (2013).
22. Galve, A. *et al.* Copolyimide mixed matrix membranes with oriented microporous titanosilicate JDF-L1 sheet particles. *J. Membr. Sci.* **370,** 131–140 (2011).
23. Aroon, M. A., Ismail, A. F., Matsuura, T. & Montazer-Rahmati, M. M. Performance studies of mixed matrix membranes for gas separation: A review. *Sep. Purif. Technol.* **75,** 229–242 (2010).
24. Bertelle, S., Gupta, T., Roizard, D., Vallières, C. & Favre, E. Study of polymer-carbon mixed matrix membranes for CO_2 separation from flue gas. *Desalination* **199,** 401–402 (2006).
25. Checchetto, R., Miotello, A., Nicolais, L. & Carotenuto, G. Gas transport through nanocomposite membrane composed by polyethylene with dispersed graphite nanoplatelets. *J. Membr. Sci.* **463,** 196–204 (2014).
26. Leenaerts, O., Partoens, B. & Peeters, F. M. Graphene: A perfect nanoballoon. *Appl. Phys. Lett.* **93,** 193107 (2008).
27. Bunch, J. S. *et al.* Impermeable atomic membranes from graphene sheets. *Nano Lett.* **8,** 2458–2462 (2008).
28. Zhang, W. D., Shen, L., Phang, I. Y. & Liu, T. Carbon nanotubes reinforced Nylon-6 composite prepared by simple melt-compounding. *Macromolecules* **37,** 256–259 (2004).
29. Paiva, M. C. *et al.* Mechanical and morphological characterization of polymer-carbon nanocomposites from functionalized carbon nanotubes. *Carbon* **42,** 2849–2854 (2004).
30. Liu, L., Barber, A. H., Nuriel, S. & Wagner, H. D. Mechanical properties of functionalized single-walled carbon-nanotube/poly(vinyl alcohol) nanocomposites. *Adv. Funct. Mater.* **15,** 975–980 (2005).
31. Chen, I.-W. P., Jhou, S.-H. S. & Chen, Y.-W. Preparation of high-quality graphene sheets and their applications in highly conductive papers and a high-performance electromechanical actuator. *J. Mater. Chem. C.* **1,** 5970–5975 (2013).
32. Wang, Y. *et al.* Raman studies of monolayer graphene: The substrate effect. *J. Phys. Chem. C.* **112,** 10637–10640 (2008).
33. Stankovich, S. *et al.* Synthesis of graphene-based nanosheets via chemical reduction of exfoliated graphite oxide. *Carbon* **45,** 1558–1565 (2007).
34. Stankovich, S., Piner, R. D., Nguyen, S. T. & Ruoff, R. S. Synthesis and exfoliation of isocyanate-treated graphene oxide nanoplatelets. *Carbon* **44,** 3342–3347 (2006).
35. Fernández-Merino, M. J. *et al.* Vitamin C is an ideal substitute for hydrazine in the reduction of graphene oxide suspensions. *J. Phys. Chem. C.* **114,** 6426–6432 (2010).
36. Yang, D. *et al.* Chemical analysis of graphene oxide films after heat and chemical treatments by X-ray photoelectron and Micro-Raman spectroscopy. *Carbon* **47,** 145–152 (2009).
37. Dervishi, E. *et al.* Large-scale graphene production by RF-cCVD method. *Chem. Commun.* **27,** 4061–4063 (2009).
38. Bruno, L. *et al.* Temperature and time effects on the structural properties of a non-aqueous ethyl cellulose topical drug delivery system. *Carbohyd. Polym.* **86,** 644–651 (2011).
39. Bruno, L., Kasapis, S. & Heng, P. W. S. Effect of hydration on the structure of non-aqueous ethyl cellulose/propylene glycol dicaprylate gels. *Int. J. Biol. Macromol.* **50,** 385–392 (2012).
40. Xu, J.-Z., Zhong. G.-J., Hsiao, B. S., Fu, Q. & Li, Z.-M. Low-dimensional carbonaceous nanofiller induced polymer crystallization. *Prog. Polym. Sci.* **39,** 555–593 (2014).
41. Ismail, A. F. *et al.* Gas separation performance of polyethersulfone/ multi-walled carbon nanotubes mixed matrix membranes. *Sep. Purif. Technol.* **80,** 20–31 (2011).
42. Wu, H., Tang, B. & Wu, P. Development of novel SiO_2-GO nanohybrid/ polysulfone membrane with enhanced performance. *J. Membr. Sci.* **45,** 194–102 (2014).
43. May, P., Khan, U., O'Neill, A. & Coleman, J. N. Approaching the theoretical limit for reinforcing polymers with graphene. *J. Mater. Chem.* **22,** 1278–1282 (2012).
44. Cheng, S., Chen, X., Hsuan, Y. G. & Li, C. Y. Reduced graphene oxide induced polyethylene crystallization in solution and composites. *Macromolecules* **45,** 993–1000 (2011).
45. Xu, J.-Z. *et al.* Graphene oxide nanosheet induced intrachain conformational ordering in a semicrystalline polymer. *J. Phys. Chem. Lett.* **3,** 530–535 (2012).
46. Wang, M.-J. Effect of polymer-filler and filler-filler interactions on dynamic properties of filled vulcanizates. *Rubber. Chem. Technol.* **71,** 520–589 (1998).
47. Zhao, Q. *et al.* Bio-inspired polyelectrolyte complex/graphene oxide nanocomposite membranes with enhanced tensile strength and ultra-low gas permeability. *Polym. Chem.* **4,** 4298–4302 (2013).
48. Tsai, M.-H., Tseng, I.-H., Liao, Y.-F. & Chiang, J.-C. Transparent polyimide nanocomposites with improved moisture barrier using graphene. *Polym. Int.* **62,** 1302–1309 (2013).
49. Scherillo, G. *et al.* Tailoring assembly of reduced graphene oxide nanosheets to control gas barrier properties of natural rubber nanocomposites. *L. ACS Appl. Mater. Interfaces* **6,** 2230–2234 (2014).
50. Koolivand, H. *et al.* Functionalized graphene oxide/polyimide nanocomposites as highly CO_2-selective membranes. *J. Polym. Res.* **21,** 599 (2014).
51. Sridhar, S. & Khan, A. A. Simulation studies for the separation of propylene and propane by ethyl cellulose membrane. *J. Membr. Sci.* **159,** 209–219 (1999).
52. Lin, H., Van Wagner, E., Raharjo, R., Freeman, B. D. & Roman, I. High-performance polymer membranes for natural-gas sweetening. *Adv. Mater.* (*Weinheim, Ger.*) **18,** 39–44 (2006).
53. Du, N., Park, H. B., Dal-Cin, M. M. & Guiver, M. D. Advances in high permeability polymeric membrane materials for CO_2 separations. *Energy Environ. Sci.* **5,** 7306–7322 (2012).
54. Lin, H. *et al.* Dehydration of natural gas using membranes. Part I: Composite membranes. *J. Membr. Sci.* **70–81**, 413–414 (2012).
55. Matteucci, S., Yampolskii, Y., Freeman, B. D. & Pinnau, I. Transport of gases and vapors in glassy and rubbery polymers. *John Wiley & Sons: New York* (2006).
56. Sadeghia, M. *et al.* Gas permeation properties of ethylene vinyl acetate-silica nanocomposite membranes. *J. Membr. Sci.* **322,** 423–428 (2008).

Acknowledgements
The authors gratefully acknowledge the financial support from the National Natural Science Foundation of China (No. 21406268), the Shandong Provincial Natural Science Foundation (No. ZR2014BM005) and the Fundamental Research Funds for the Central Universities (No. 14CX05034A).

Author Contributions
H.S. and B.Y. designed the research plan and synthesized the nanoporous graphene nanosheets using the facile hydrothermal treatment. T.W. and Y.X. conducted the fabrication of MMMs and C_3H_6/C_3H_8 separation experiments. Q.J.N., P.L. and Y.K. performed the characterization of graphene nanosheets and MMMs. H.S. and B.Y. analyzed the data and interpreted the results. B.Y. and H.S. drafted the manuscript, and all authors revised the manuscript.

Additional Information
Supplementary information accompanies this paper at http://www.nature.com/srep

Competing financial interests: The authors declare no competing financial interests.

How to cite this article: Yuan, B. *et al.* Propylene/propane permeation properties of ethyl cellulose (EC) mixed matrix membranes fabricated by incorporation of nanoporous graphene nanosheets. *Sci. Rep.* **6**, 28509; doi: 10.1038/srep28509 (2016).